www.czasopisma.pan.pl PAN www.journals.pan.pl

Opto-Electronics Review 25 (2017) 318–325

Contents lists available at ScienceDirect

Opto-Electronics Review

journal homepage: http://www.journals.elsevier.com/opto-electronics review

Microwave metamaterial absorber for sensing applications

M. Bakır[a], M. Karaaslan[b], E. Unal[b], O. Akgol[b], C. Sabah[c,d,*]

[a] Department of Computer Engineering, Faculty of Engineering and Architecture, Bozok University, Yozgat, 66200, Turkey
[b] Department of Electrical and Electronics Engineering, Iskenderun Technical University, Iskenderun, Hatay 31200, Turkey
[c] Department of Electrical and Electronics Engineering, Middle East Technical University – Northern Cyprus Campus (METU-NCC), Kalkanli, Guzelyurt, 99738, TRNC/Mersin 10, Turkey
[d] Kalkanli Technology Valley, Middle East Technical University – Northern Cyprus Campus (METU-NCC), Kalkanlı, Guzelyurt, 99738, TRNC/Mersin 10, Turkey

ARTICLE INFO

Article history:
Received 27 May 2017
Received in revised form
18 September 2017
Accepted 17 October 2017
Available online 9 November 2017

Keywords:
Metamaterial
Absorber
Microwave
Sensor

ABSTRACT

A metamaterial absorber (MA) based sensor is designed and analysed for various important applications including pressure, temperature, density, and humidity sensing. Material parameters, as well as equivalent circuit model have been extracted and explained. After obtaining a perfect absorption (PA) at around 6.46 GHz and 7.68 GHz, surface current distributions at resonance points have been explained. Since bandwidth and applicability to different sensor applications are important for metamaterial sensor applications, we have realized distinctive sensor demonstrations for pressure, temperature, moisture content and density and the obtained results have been compared with the current literature. The proposed structure uses the changes on the overall system resonance frequency which is caused by the sensor layer's dielectric constant that varies depending on the electromagnetic behaviour of the sample placed in. This model can be adapted to be used in sensor applications including industrial, medical and agricultural products.

1. Introduction

Metamaterials (MTMs) are such engineered structures that possess extraordinary features such as backward propagation, negative permittivity and/or permeability. They allow researchers to explore many interesting areas [1–6]. MTM sensors offer higher sensitivity and resolution compared to the traditional structures due to their strong localization of fields [7]. They also reduce the sensor size compared to a regular structure that is less proportional to the operating frequency. Hence, MTMs have been extensively used in sensor applications for the past decade. For example, Chen et al. [7], presented the recent progress concerning metamaterials-based sensing, and detailed reviews of the principle, detecting process and sensitivity of three distinct types of sensors based on metamaterials. Lee et al. [8] reviewed the MTM and metasurfaces for sensor applications. Cherifi and Bauhafs [9] investigated a potential of SPR sensors based on multilayer interfaces with gold and LHM for biosensing applications. Upadhyay et al. [10] conducted a study for sensitivity estimation of metamaterial loaded planar waveguide sensors. Biosensors, material investigation sensors, strain sensors, environmental [11–14] and agricultural product sensors [15–18] are the most popular type of MTM sensors. One of the fundamental properties of MTM sensors is that they concentrate and use the electrical specifications of materials [19,20]. Since the dielectric properties of materials exposed to electromagnetic field will affect the incident wave and current depending on the material type [20–24], these effects are beneficially used by scientists to develop MTM sensor applications and designs [25–29].

In this manuscript, a concept study which is covering both MA and MTM sensor studies in C band is developed to provide high resolution sensing in temperature, humidity, pressure and density. Although there is another study for the combination of MA with MTM sensor in X band waveguide in literature [30], this type of waveguide applications is restricted by their small dimensions. Hence, this structure is designed to operate in C band between 5 GHz – 8 GHz within the periodic boundary conditions. Sensor layer is placed between the resonator part and copper plate in this proposed topology. Variation in a sensor layer leads to shifts in the resonance frequency of the proposed sensor system. Therefore, frequency shifts measured from the reflection pattern can be used for sensing physical and biological parameters of the sample under test (SUT). Resonance frequency shift in this study is based on the change of dielectric constant value of the sensor layer which is influenced by the electric field. Therefore, the entire system can be regarded as being non-destructive and real time. Sensor out-

* Corresponding author at: Department of Electrical and Electronics Engineering, Middle East Technical University – Northern Cyprus Campus (METU-NCC), Kalkanli, Guzelyurt, 99738, TRNC/Mersin 10, Turkey.
E-mail address: sabah@metu.edu.tr (C. Sabah).

https://doi.org/10.1016/j.opelre.2017.10.002
1230-3402/

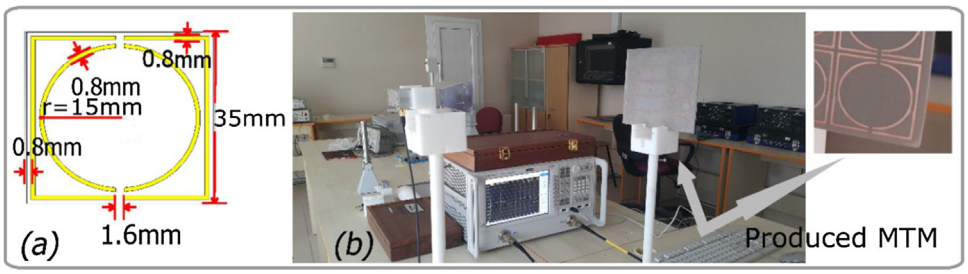

Fig. 1. (a) 35 mm x 35 mm unit Cell of the proposed MA based sensor structure which is composed from square and ring resonators cell; (b) experimental setup for absorber and sensor applications in free space testing together with produced MTM.

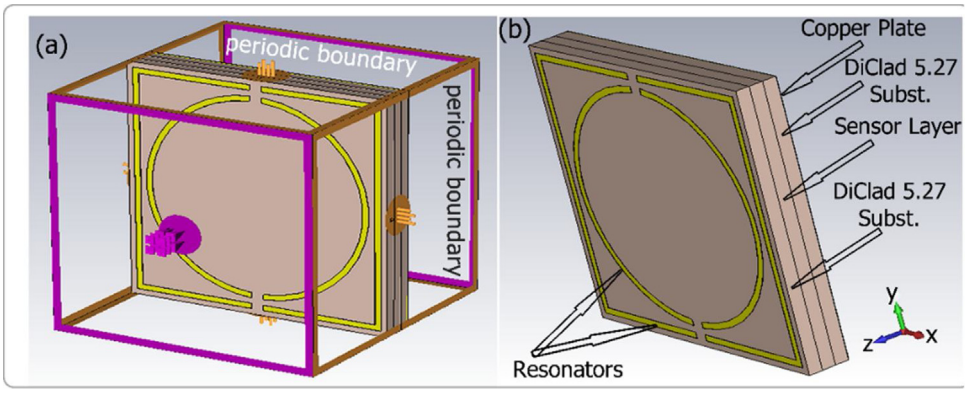

Fig. 2. (a) The proposed structure for sensing configuration showing layers and boundary conditions in X, Y axis; (b) explanation of layers in the sensor configuration of the proposed structure.

put provides information about the sample, in particular about the complex permittivity of the sample that can be applied for analysis and recognition. Although today's sensors (both analogue and digital types) are readily available with very low cost, good accuracy, and easier to carry out the measurement results, the proposed MA based sensor provides different approach and multipurpose application types to researchers due to its practical structure. Sandwich type sensor layer can be applied for biosensor and food related heating or cooling applications of powders for complex permittivity measurements. In order to exemplify this type of applications, temperature, moisture and density applications have been proposed by using recent studies in the literature [31–36].

2. Design details

Proposed MTM structure as introduced in Fig. 1 is composed of two resonators; one of them is a square and the other one is a ring shaped inclusion which incorporates two splits. Resonators are made of copper elements with the conductivity of 5.8×10^7 S/m, lossy Arlon DiClad 527 from Rogerscorp material is used as a substrate with a thickness of 1.6 mm, dielectric constant of 2.50 and loss tangent of 0.0002. Square and ring resonators have a thickness of 0.8 mm and the distance between the square resonator and the unit cell edge is also 0.8 mm. Split width on the resonators are chosen as 1.6 mm and the external radius of the split ring resonator is 15 mm. These dimensions are especially chosen by evaluating parametric studies to ensure the best numerical and experimental results. Design is produced by using a CNC controlled machine and experimental tests are realized by using a horn antenna connected to a 42.5 GHz VNA as shown in Fig. 1(b). For absorber and sensor configuration tests, single port with time gating in VNA is used (single port Tx-Rx) for feeding the horn antenna which transmits linearly polarized electromagnetic waves with normal incidence to the manufactured test sample which is compromised from 5×5 unit cells.

As it is explained in the following sections, the proposed design is tested numerically and experimentally for absorber and sensor applications. In the absorber configuration case, copper plate is used behind the dielectric substrate that supports resonators. For the sensor configuration case, a copper plate is not used behind the resonators' substrate and the sensor layer is placed behind the substrate. In order to show the absorption characteristics, a dielectric substrate (DiClad 5.27) which is backed by copper is placed behind the sensor layer as shown in Figs. 2(a) and 2(b) . For sensor and absorber applications, periodical boundary conditions are applied along $-x$ and $-y$ axes while open add space boundary is assigned along $+z$ direction and the wave is applied along $-z$ axes. CST Microwave Studio based on Finite integration technique (FIT) is used for a numerical analysis. The boundaries in CST are defined as Periodic, Periodic, Open Add Space along x, y, and z axes, respectively. This type of selection provides normal incidence wave, in other words Transverse electromagnetic wave (TEM) propagation. For the simulation and test, we selected the incident angle direction as $-$Z and polarization angle as of 90°. In this type of application, electric field vector is in Y direction while magnetic field vector is in X direction as in Fig. 2. Frequency domain solver in CST Microwave Studio is used as a solver type throughout the paper. The novel geometry is specifically designed to increase mutual and self-coupling effects. Dielectric constant of the sensor layer directly changes these effects which results in a resonance shift of the reflection coefficient. These shifts in the resonance frequency can be explained by $1/\sqrt{LC}$ expression.

The microwave sensor structure can be modelled by an electrical circuit representation which is composed of inductances, resistances and capacitances. It can be assumed that self-inductance of MTM structure is constant since the self-inductance $\left(L_{self}\right)$ of the circuit is only related to the metallic path lengths and incident signal wavelength. The change of dielectric constant in the sensing layer does not change the self-inductance of MTM structure on the front side due to the lack of magnetic effects. Since the

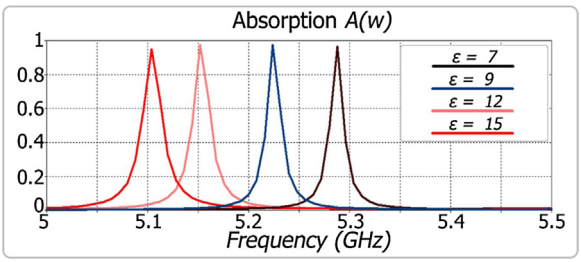

Fig. 3. Absorption A(w) *vs.* frequency for different dielectric constant values.

Table 1
The rapeseed temperature, complex permittivity and resulting resonance frequency for the proposed MA based sensor application. Necessary temperature and complex permittivity data is taken from Ref. [34].

The Rapeseed Temperature	ε'	ε''	Loss Tangent	Resonance Frequency (GHz)
20 °C	5	2	0.40	6.10
40 °C	6.8	2.1	0.30	6.00
60 °C	8	2.3	0.28	5.95

thickness of a sandwiched layer region is constant, mutual inductance between metallic ground plane and MTM structure is stable. In this respect, the individual mutual inductances are also constant. The self-capacitance (C_{self}) of the MTM structure is affected from both gap capacitances in the square and circular paths and capacitances among the outer and inner paths ($C = \kappa\varepsilon_0 A/d$). This equation represents the capacitance value of the parallel plate capacitors according to the given amount of charge (κ), area of the parallel plate capacitor (A) and distance of parallel plated conductors (d). By keeping A and d values constant, capacitance values increase as the dielectric permittivity of the sensor layer increases and, $1/\sqrt{LC}$ resonance frequency also shifts backward as in the tank circuit equations and vice versa.

It is well known that the effective dielectric constant of the sensing layer ε_{eff} (sub) is related with the permittivity of the sensing material. In addition, the effective dielectric constant changes self-capacitance (C_{self}) of the MTM structure on the front side. Hence, self-capacitance is proportional with thickness and relative permittivity of the sensing layer. The mutual capacitance refers to the relationship between MTM on the front side and backside metallic layer and can be defined by an equivalent circuit model of capacitance of MTM structure and a capacitance of the sensor layer:

$$\frac{1}{C_{mut}} = \frac{1}{C_{MTM}} + \frac{1}{C_{int}}, \tag{1}$$

where C_{MTM} and C_{int} denote the capacitances of MTM on the front side and of the sensing layer, respectively. The total capacitances of the system are directly related with both mutual and self-capacitances. The resonance of the system is observed for equivalent values of total inductance and capacitance. At the resonance frequency, the intrinsic impedance of the system is almost similar to the free space impedance and total internal penetration is provided to obtain higher absorption values.

In order to show the underlying physics of the proposed structure, the following simulation study is presented. For this purpose, sensor layer thickness is set to 1.6 mm as in the proposed applications in this study and the S_{11} Spectra is simulated for different values of the sensor layer dielectric constant as ε=7, 9, 12 and 15 and the results are plotted in Fig. 3. The resonance frequency shifts backward as the dielectric constant of the sensor layer is increased due to capacitive effects of the sensor layer. Variation of the resonance frequency according to the sensor layer dielectric constant is given in Table 1. Total bandwidth is of 180 MHz as the dielectric constant increases from 7 to 15 with absorption rates bigger than 92%. This graph is also important for the scientists who want to use in the future for different applications. The absorption mechanism of the overall structure can be explained in the light of impedance matching of free space from which the incident wave comes and with the intrinsic impedance of the proposed MA. It is well known that the effectiveness of an absorber is directly related with both impedance matching of the surfaces at resonance frequency to provide exact penetration of incident wave and backside metallic ground plane to restrain the wave in the MA. Both conditions must be satisfied at the resonance frequency.

In order to show the effective material parameters epsilon, mu and refractive index, the following graph is plotted between 6 GHz and 8 GHz. As presented in Fig. 4(a) , negative values of refractive index at resonance points can be seen. Equivalent circuit model of the proposed sensor structure is presented in Fig. 4(b). The resistors

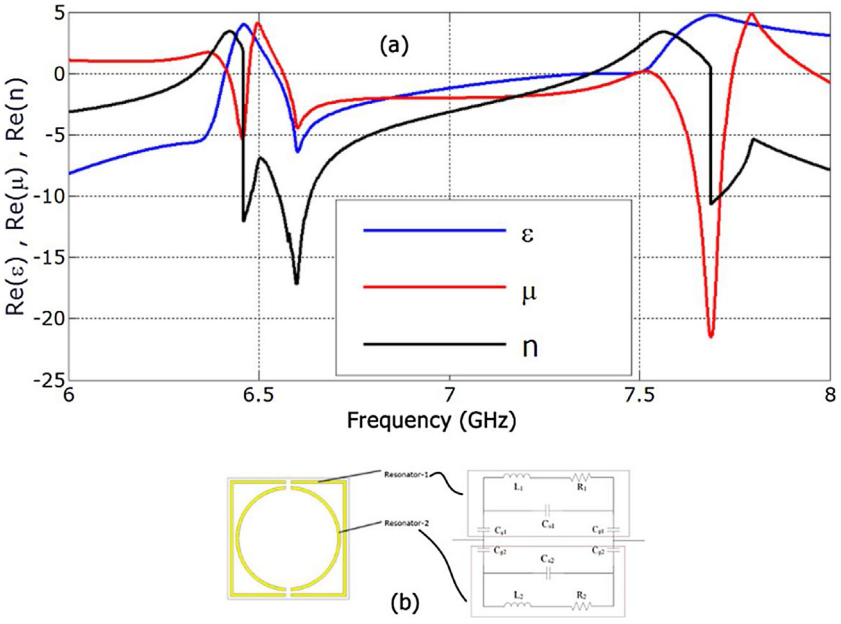

Fig. 4. (a) Extracted effective material parameters; (b) equivalent circuit model of the proposed structure.

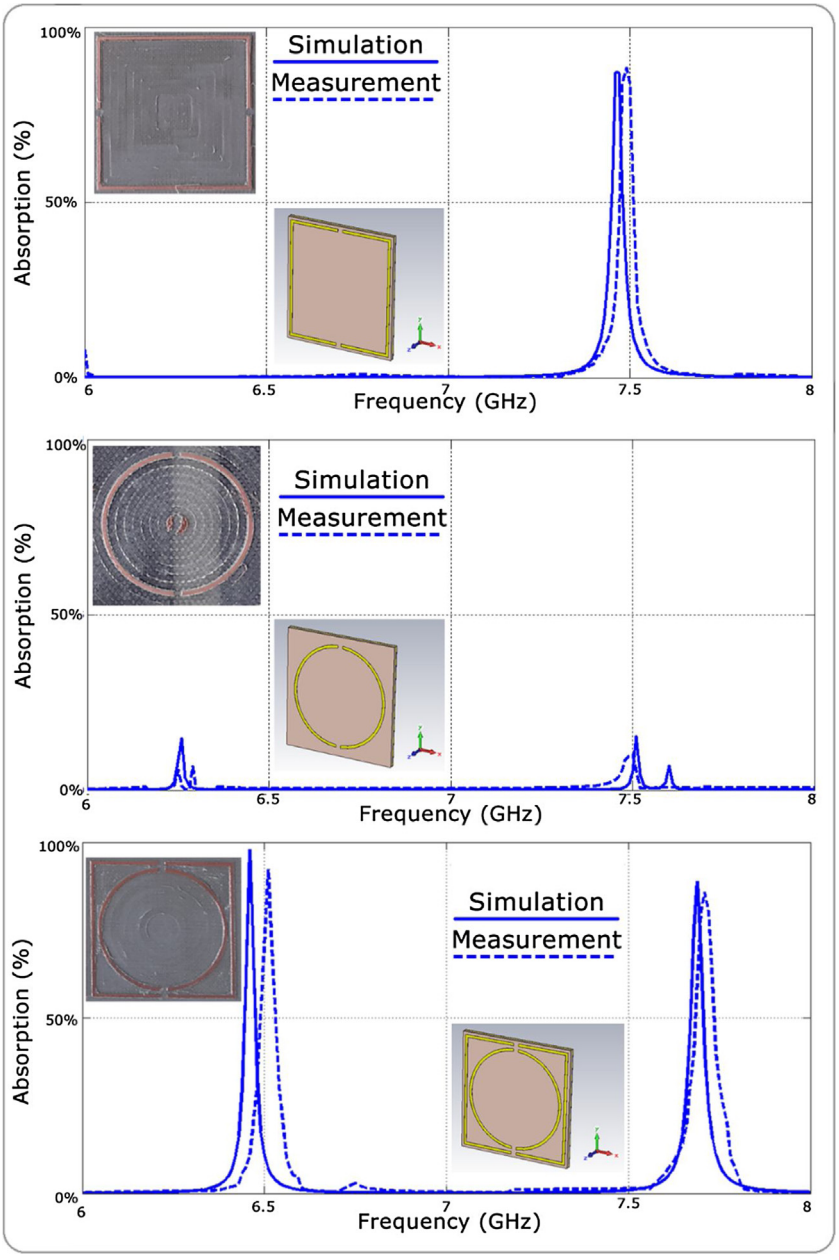

Fig. 5. In order to show the effects of the resonators, three structures which are composed from 5×5 unit cells have been manufactured and tested under the periodic boundary conditions for absorber configuration. Absorption *vs.* frequency of the (a) structure which has a square split ring resonator, (b), structure which has a split ring resonator, (c) proposed structure that has a split square ring and a split ring resonator.

R1 and R2 indicate total power loss in the resonator parts of the proposed structure [31]. The overall effective inductance L1 and L2 consist of a unit cell resonator with mutual inductance. Cs1 and Cs2 are originated from mutual capacitance between the neighbouring unit cells [32]. Cg1 and Cg2 are the effects of capacitive gap placed in inner and outer resonator of the structure, respectively and they provide charge accumulation by the external field.

3. Metamaterial absorber and metamaterial sensor

3.1. MTM absorber application

Since the proposed MTM sensor applications are based on the absorber mechanism, we physically produced, numerically and experimentally verified the absorber application. For absorber applications, copper plate is placed behind the dielectric of the resonators and experimental verification of absorber is tested by using horn antennas. Numerical verification is realized by using CST microwave studio under periodic boundary conditions. It is known that the essential requirement of an absorber is to confine the penetrated energy in the structure. The reflected and transmitted waves have to be minimized ($R(\omega)\&T(w) \rightarrow 0$) so that these waves should be as small as possible in order to realize perfect absorption. Absorption which is related to the angular frequency can be calculated by the equation of:

$$A(w) = 1 - R(w) - T(w), \tag{2}$$

where, $A(w)$, $R(\omega) = |S_{11}|^2$ and $T(\omega) = |S_{21}|^2$ are the magnitude of the absorption, reflection and transmission corresponding to a certain frequency range, respectively. Due to the continuous metal plate, transmission is not allowed so it would be close to zero ideally. Therefore, only the reflection value of the overall structure

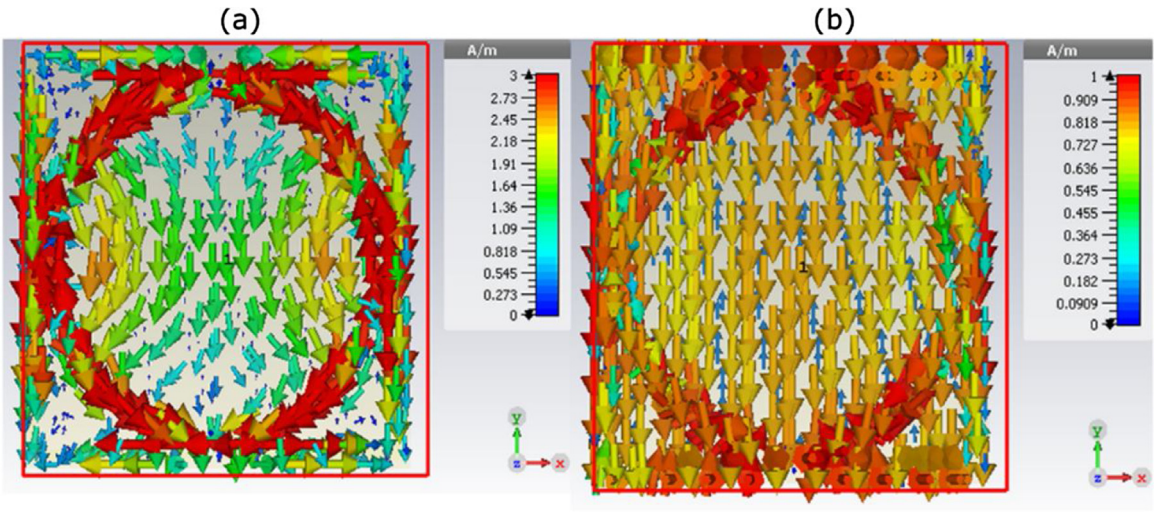

Fig. 6. Simulated surface current distribution at the absorption frequency of (a) 6.46 GHz, (b) 7.68 GHz for the proposed structure.

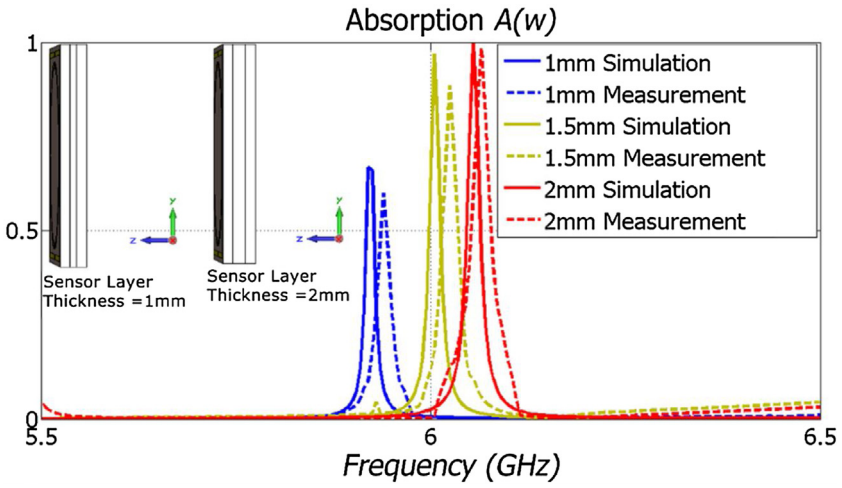

Fig. 7. Numerical simulation and experimental test results: comparison for pressure sensor configuration between 1 and 2 mm.

needs to be investigated which is directly related with S_{11}. As a result, the absorption can be calculated as:

$$A(w) = 1 - R(w). \tag{3}$$

The physics behind using two resonators in this study is to realize high efficient sensor applications by using Metamaterial Absorber (MA). Using two resonators in front of the proposed MA structure provides more absorption values which increases sensitivity. The other reason of using second resonator on the front side of the structure is for tuning purposes. By using second resonator, we will increase the absorption and we can change the absorption frequency according to the place and dimensions of the split. In order to show the importance of using two resonators in front the structure, following simulation and experimental graph is prepared. Resonators are placed in the front side which supported by a dielectric substrate. After that, the copper plate is placed behind the dielectric substrate to realize an absorber configuration without sensor layer. When we compare the simulated and experimental absorption graph of the structure which has square split ring resonator as plotted in Fig. 5(a) , we only see a single resonance around 7.4 GHz. If only split ring resonator has been used in the proposed structure as plotted in Fig. 5(b), we will not get a significant absorption. However, if we use both square and split ring resonators as in the proposed structure, we have two resonance points between 6 GHz and 8 GHz as shown in Fig. 5(c)As seen from the following figure, square ring resonator is directly affecting the resonance frequencies and the absorption level. Without split ring resonator, absorption occurs at around 7.4 GHz with a smaller absorption level. These effects are caused by mutual and self-inductance with capacitance values of resonators. Manufactured samples and experimental results are also compliant with the simulated results. These results are presented to show the advantageous sides of the proposed structure.

As presented in Fig. 5(c), two resonances are observed at 6.46 GHz and 7.68 GHz for the proposed structure. Resonance frequencies are located in the upper half of the C-band and dual resonance characteristics are sufficient to absorb electromagnetic energy. When numerical results are compared with the experimental results, a tiny shift is seen in the resonant frequency which is due to calibration, fabrication errors and non-ideal measurement conditions and tools (cables, adaptors, etc.). Measured absorption level is also smaller than that of the simulation due to the same reasons.

In order to explain the physical properties of the structure, surface current distribution is simulated at 6.46 GHz and 7.68 GHz as shown in Fig. 6. Since electric field vector is in the Y axis direction, it is strongly coupled with the splits and provides an independent electric response making them to be seen as a dipole. As a result, the

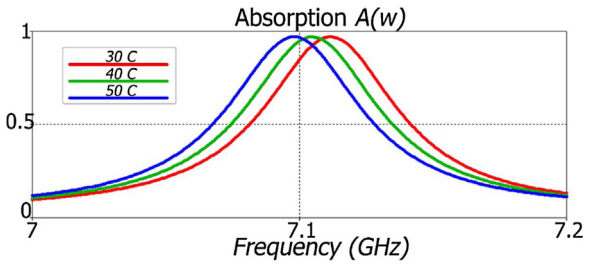

Fig. 8. Absorption for the Marrowbone Temperature Sensor Configuration between 7 GHz and 7.2 GHz.

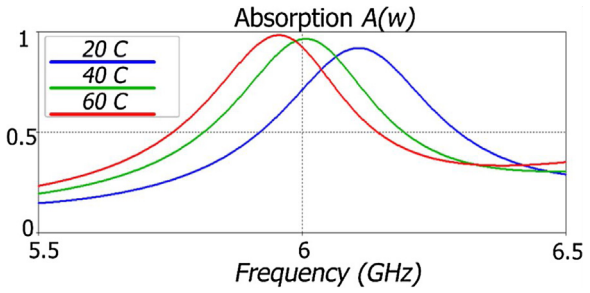

Fig. 9. Absorption for the Rapeseed Temperature Sensor Configuration between 5.5 GHz and 6.5 GHz, 150 MHz bandwidth is observed between 20 °C and 60 °C rapeseed.

surface charge oscilates along the external electrical field. This electric response excites free electrons as a surface currents from upside to downside of the strips. For this reason, magnetic dipole moment due to the surface current charges induces magnetic response. This magnetic response, consequently, causes a resonant absorption. Moreover, there are parallel and anti-parallel surface currents on the structure. Parallel currents induce an electric field, whereas the anti-parallel currents induce a magnetic field. These responses couple with E and H components of the indicent EM wave and produce a strong localized EM field at the resonance frequency. While strong resonance at 6.46 GHz causes surface currents at left and right of the resonators, we can see that small surface currents through the resonators as shown in Fig. 6(b).

3.2. Pressure sensor application

The first sensor application of the proposed sensor configuration defined in Fig. 2 is a pressure sensor. It is simulated and experimentally tested by changing the sensor layer's thickness up and down which corresponds to a pressure alteration. Three different air cushions that have been taken as samples which are of 1 mm, 1.5 mm and 2 mm to show reflection coefficient both numerically and experimentally are presented in Fig. 7. Three different air cushions are particularly chosen to show linearity. Since capacitance is inversely proportional with plate distances, the increment of the distance decreases capacitance value and resonance frequency shifts upward $(1/\sqrt{LC})$. Absorption $[A(w)]$ term is the main criteria for all sensor applications in this study, since air is an isolating material and its thickness affects $A(w)$ term. Absorption frequencies for the sensor layer with a thickness of 1 mm, 1.5 mm and 2 mm have been defined as 5.92 GHz, 6.00 GHz and 6.05 GHz, respectively as shown in Fig. 7. The corresponding absorption values are of 0.77, 0.97, 0.99 at the resonance frequencies of 5.92, 6.00 and 6.05 GHz, respectively. Better absorption values are observed for the layer thickness of 1.5 and 2.0 mm. Figure 7 also shows that a 1 mm change in the sensor layer thickness results in a shift of 130 MHz in the resonance frequency which proves that the sensor application based on this absorber is highly sensitive to the

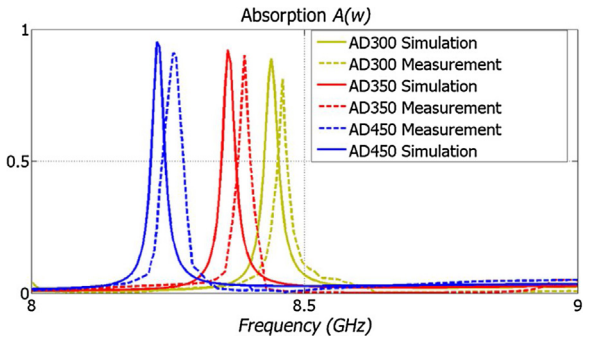

Fig. 10. MA Based density sensor: numerical and experimental result comparison for Arlon type AD300, AD 350 and AD450 materials.

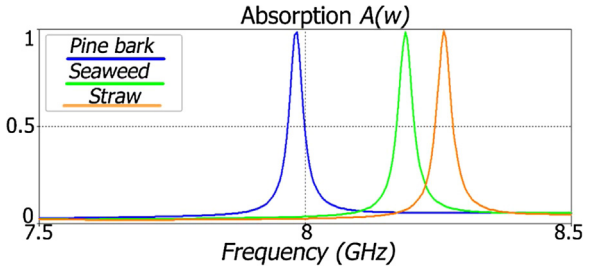

Fig. 11. MA Based density sensor simulation results for pine bark, seaweed and straw between 7.5 and 8.5 GHz.

changes in the sensor layer thickness. There are small differences between numerical and experimental results which come from the calibration and fabrication errors as mentioned before. The proposed sensor can be realized for only one resonant frequency by replacing a varicap across the gaps. By tuning the capacitance value, only one resonance frequency with the same absorption value can be obtained.

3.3. Temperature sensor application

In order to demonstrate the usefulness of the proposed structure in bio-sensor application and agricultural products, two numerical studies are realized. The first study is related with a marrowbone temperature sensing, and the second study is related with a rapeseed temperature sensing. Temperature sensing is important in order to understand how biological tissue temperature is affected from electromagnetic waves being used in static absorption rate (SAR) or curative waves testing. Heating properties of biological tissues are generally related with liquid ratios but absorption properties of biological tissues are directly proportional with variable permittivity and layer numbers of biological tissues. For this reason, in order to investigate the EM absorption rate of the biological tissues, it is critical to monitor the temperature changes. In this respect, the sensor layer thickness is kept constant at 1.6 mm and this layer is composed of marrowbone with different temperatures in the simulation case. Marrowbone's temperature and complex permittivity values are taken from a related study in the literature [33]. Any changes in temperature will result in variations of complex relative permittivity of marrowbone causing a shift in resonant frequency of the system. Temperature sensor simulation is performed by using 3 different temperature values of 30 °C, 40 °C and 50 °C. The real parts of the relative permittivity ε' corresponding to the temperatures mentioned above are 6.19, 6.30, 6.40, respectively. Using these values in the simulation, the resonance frequencies are found to be 7.11, 7.10, 7.09 GHz, respectively (Fig. 8). Absorption values are approximately constant at a (0.97) level for each of the three temperature values. There is

Table 2
Pine bark, seaweed and straw density, complex permittivity and resulting resonance frequency table. Related data is taken from Ref. [36].

Material and Solid Density (gr/cm3)	ε'	ε''	Loss Tangent	Resonance Frequency (GHz)
Pine bark – 1.60	7.20	0.04	0.009	7.98
Seaweed – 1.73	4.89	0.05	0.01	8.18
Straw – 1.82	4.26	0.08	0.01	8.26

approximately a linear relationship between the temperature and resonance frequency between 7 – 7.2 GHz. That is, for every 10 °C change in temperature, 10 MHz shift occurs in the resonance frequency.

Another important temperature sensor application is rapeseed temperature sensing for showing agricultural product temperature application. Rapeseed is one of the oilseed crops that have been grown almost everywhere in the world as a source of edible and non-edible oils, vegetable, fodder, manure and condiment. After extracting oil from seeds, the remaining residue can be used as animal feed or fertilizer together with an option as biodiesel production due to its advantageous in low carbon dioxide emission and biodegradability [34]. The dielectric properties of food materials are important in order to understand their behaviour when they are subjected to high frequency electromagnetic fields in the process of microwave cooking or in other processes which involve radio frequency (RF) or microwave dielectric heating [34]. These properties can also help to assess the quality of food materials by using RF and microwave instruments. We have taken 20 °C, 40 °C and 60 °C rapeseed as samples and their corresponding complex permittivity values are presented in Table 1. Since the proposed study is based on a change in the complex permittivity of the sensor layer, it can be used as a temperature sensor since material complex permittivity values are changing by temperature or other environmental effects. When changing the complex permittivity values according to rapeseed complex permittivity values, simulation results are given in Fig. 9 between 5.5 and 6.5 GHz. 150 MHz bandwidth is observed when the temperature of the rapeseed increased from 20 °C to 60 °C and this bandwidth is two times greater than the bandwidth in Ref. [35]. This demonstration can be applied to other industrial and scientific biosensor or temperature examples if the complex permittivity is changing by temperature.

3.4. Density Sensor Application

Sensor layer can be used to detect the density of a material if it is properly configured. In this part of study, the sensor layer is assumed to be filled with such materials that have different density values. Sensor layer thickness is again 1.6 mm for both numerical and experimental parts of this illustration. As a beginning, three different materials known as Arlon AD300, Arlon AD350 and Arlon AD 450 are used in the sensor layer for simulation and experimental validation. Numerical and experimental results are presented in Fig. 10. Resonance frequencies are of 8.44, 8.36, 8.23 GHz for AD 300, AD350 and AD450, respectively. When AD450 type material is used in the sensor layer, the maximum absorption value of 0.97 is obtained. The dielectric constants are of 3, 3.5, 4.5 for AD 300, AD350 and AD450, respectively. As seen from Fig. 10, when the dielectric constant of the material used in the sensor layer increases, the resonance frequency of the absorber based sensor shifts downward. The total shift is of about 210 MHz which shows that the absorber based sensor is highly sensitive to the changes of the dielectric constant of the sensor layer. This relationship is the basis for all sensor applications in this design. The difference between the resonance frequencies of numerical and experimental results is of about 30 MHz. Fabrication, measurement, environmental or calibration errors may cause such a difference. Due to the losses of Arlon 350, Arlon 400 and Arlon 450 material used and other production errors, amplitude of the signals have a difference of 5% since $\varepsilon = \varepsilon' - j\varepsilon''$. In this equation, losses are directly affecting the dielectric permittivity and indirectly affecting the absorption rate.

Table 3
Water content of sandy soil, dielectric constant, loss tangent and related resonance frequencies [38].

Almond Kernel Moisture Content (%)	ε'	ε''	Loss Tangent	Resonance Frequency (GHz)
8	3.75	1.3	0.34	6.21
11.9	5.1	2	0.39	6.09
15.8	7.8	2.7	0.34	5.95
19.6	9.2	3.4	0.36	5.87

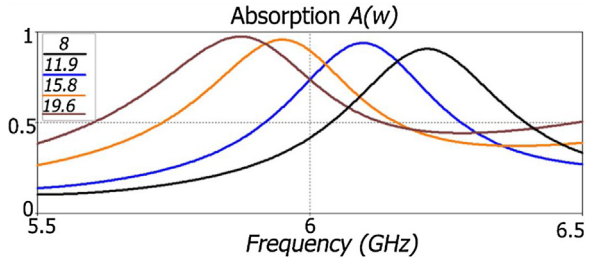

Fig. 12. Absorption for the MA Based moisture content of sand between 5.5 and 6.5 GHz.

Global challenges related with energy, sustainability, and the environmental impacts of burning fossil fuels lead to an increasing need for switching to the use of clean resources [36]. One of the suggestions to solve this problem is Bio-oil, pine bark, seaweed and straw can be used as source of bio oil and their density values with complex permittivity have been researched in the literature [36]. In this part of the simulation, sensor layer is assumed to be composes from these materials without changing its dimensions and absorption rate simulated according to them. Density values and complex permittivity values of these materials with corresponding resonance frequencies are summarized in Table 2. As seen from Fig. 11, 262 MHz bandwidth observed according to the change of density by 22 g/cm^3. This value is greater than the bandwidth obtained in Ref. [37] when density and resonance frequency values are taken as sample.

3.5. Moisture sensor application

Another sets of simulation designed to illustrate the proposed design is related with moisture sensing. Moisture values of agricultural products and textile products are crucial since it is affecting the lifetime of the products. For this purpose, almond kernel moisture content versus absorption frequency is simulated. As presented in Table 3, four different almond kernels are taken as sample from the literature [38]. While their moisture contents are of 8%, 11.9%, 15.8% and 19.6%, the corresponding dielectric constants are of 3.75, 5.1, 7.8 and 9.2, respectively. Without changing the dimensions of the sensor layer, it is assumed to be composed of almond kernels with different moisture contents. Using the data given in Table III, S parameters and absorption values are calculated by CST Microwave Studio. The absorption values are then plotted as a function of frequency as shown in Fig. 12. The total shift in the resonance frequency is found as of 340 MHz as the moisture content of almond kernel increases from 8% to 19.6%. In this application, the maximum value of the absorption is of about 97% and similar absorption rates are observed due to similar tangent losses.

4. Conclusions

This study focuses on multi-functional sensor applications based on MA. The sensing properties of the suggested sensor design are presented for pressure, temperature, density, and humidity. Surface current distributions, material parameters and equivalent circuit model of the proposed structure. Another sets of simulation designed to illustrate the proposed design is related with moisture sensing. Moisture values of agricultural products and textile products are crucial since it is affecting the lifetime of the products. For this purpose, almond kernel moisture content *vs.* absorption frequency is simulated. As presented in Table 3, four different almond kernels are taken as sample from the literature [38]. While their moisture contents are of 8%, 11.9%, 15.8% and 19.6%, the corresponding dielectric constants are of 3.75, 5.1, 7.8 and 9.2, respectively. Without changing the dimensions of the sensor layer, it is assumed to be composed of almond kernels with different moisture contents. Using the data given in Table 3, S parameters and absorption values are calculated by CST Microwave Studio. The absorption values are then plotted as a function of frequency as shown in Fig. 12. The total shift in the resonance frequency is found as of 340 MHz as the moisture content of almond kernel increases from 8% to 19.6%. In this application, the maximum value of the absorption is of about 97% and similar absorption rates are observed due to similar tangent losses.

In order to show the sensor quality of the proposed design, pressure and density sensor applications are also experimentally tested. It can be seen that the numerical results are in a good agreement with the experimental ones. Linear shifts can be seen in different sensor applications. Operation principle of the proposed MA based sensor application study depends on the sensor layer's thickness or sensor layer's dielectric properties. Therefore, different sensor application for industrial scientific and medical use can be developed if the dielectric constant value is changing.

Acknowledgements

O. Akgol, of the author acknowledges the support of TUBITAK under the Projects No. 114E295 partial support of the Turkish Academy of Sciences. The authors would like to thank Olcay Altintas for his help during the preparation of the paper. Additionally, the authors thank the anonymous reviewers for their constructive comments and suggestions to improve the paper.

References

[1] M. Zhong, Influence of dielectric layer on negative refractive index and transmission of metal – Dielectric-Metal Sandwiched Metamaterials, Chin. Opt. Lett. 12 (2014), 041601-1-041601-3.
[2] D.O. Boillat, T. Friedli, J.W. Kolar, Electronically controllable impedance for tuning of active metamaterials, IEEE J. Emerg. Sel. Top. Power Electron. 5 (3) (2017) 1404–1414.
[3] H.Y. Dong, et al., Realization of broadband acoustic metamaterial lens with quasi-conformal mapping, Appl. Phys. Express 10 (8) (2017) 087202.
[4] M. Bakir, Electromagnetic-based microfluidic sensor applications, J. Electrochem. Soc. 164 (9) (2017) B488–B494.
[5] F. Dincer, M. Karaaslan, O. Akgol, E. Unal, C. Sabah, Design of polarization-and incident angle-independent perfect metamaterial absorber with interference theory, J. Electron. Mater. 43 (2014) 3949.
[6] Y. Gang, L. Furi, Y. Jin, L. Chunya, J. Jie, Y. Jianquan, Dual-band tunable perfect metamaterial absorber in the THz range, Opt. Express 24 (2016) 1518–1527.
[7] T. Chen, S. Li, H. Sun, Metamaterials application in sensing, Sensors 12 (2012) 2742.
[8] Y. Lee, S. Kim, H. Park, B. Lee, Metamaterials and metasurfaces for sensor applications, Sensors 17 (8) (2017) 1726.
[9] A. Cherifi, B. Bauhafs, Potential of SPR sensors based on multilayer interfaces with wold and LHM for biosensing applications, Photonic Sensors 7 (33) (2017) 199–205.
[10] A. Upadhyay, Y.K. Prajapati, V. Singh, J.P. Saini, Sensitivity estimation of metamaterial loaded planar waveguide sensor, Opt. Quantum Electro. 47 (7) (2015) 2277–2287.
[11] K.V. Sreekanth, Y. Alapan, M. ElKabbash, U.A. Gurkan, D. Luca, G. Strangi, A plasmonic platform based on hyperbolic metamaterials for extreme sensitivity biosensing, Nature Mater. 15 (2016) 621–627.
[12] K. Kim, D. Lee, S. Eom, S. Lim, Stretchable metamaterial absorber using liquid metal-filled polydimethylsiloxane (PDMS), Sensors 16 (2016) 521.
[13] M.H. Zarifi, T. Thundat, M. Daneshmand, High resolution microwave microstrip resonator for sensing applications, Sens. Actuators A: Phys. 233 (2015) 224–230.
[14] A.K. Horestani, Two-dimensional alignment and displacement sensor based on movable broadside-coupled split ring resonators, Sens. Actuators A: Phys. 210 (2014) 8–24.
[15] N. Nurfatmah, N. Pauzi, A. Syafiq, A. Hazmi, H. Abdul Aziz, A.B. Zailan, Z. Indris, Frequency response and activation energy of palm-fatty acids at microwave region, Int. J. Hydrogen Energy 42 (32) (2017) 20444–20452.
[16] A.P. Franco, L.Y. Yamamoto, C.C. Tadini, J.A. Gut, Dielectric properties of green coconut water relevant to microwave processing: effect of temperature and field frequency, J. Food Eng. 155 (2015) 69–78.
[17] N. Ramly, N. Aini, N. Sahli, S. Aminuddin, M. Yahya, A. Ali, Dielectric behaviour of UV-crosslinked sulfonated poly (ether ether ketone) with methyl cellulose (SPEEK-MC) as proton exchange membrane, Int. J. Hydrogen Energy 42 (2016) 9284–9292.
[18] J. Corach, P. Sorichetti, S. Romano, Electrical properties of vegetable oils between 20 Hz and 2 MHz, Int. J. Hydrogen Energy 39 (2014) 8754–8758S.
[19] M.A. Rao, S.S. Rizvi, A.K. Datta, J. Ahmed, Engineering properties of foods, CRC press, 2014.
[20] Y. Han, J. Wang, Y. Li, Y. Hang, X. Yin, Q. Li, Circular dichroism and infrared spectroscopic characterization of secondary structure components of protein Z during mashing and boiling processes, Food Chem. 188 (2015) 201–209.
[21] H. Hu, X. Zhu, T. Hu, I.W. Cheung, S. Pan, E.C. Li-Chan, Effect of ultrasound pre-treatment on formation of transglutaminase-catalysed soy protein hydrogel as a riboflavin vehicle for functional foods, J. Funct. Foods 19 (2015) 182–193.
[22] R. Morales, K.D. Martínez, V.M.P. Ruiz-Henestrosa, A.M. Pilosof, Modification of foaming properties of soy protein isolate by high ultrasound intensity: Particle size effect, Ultrason. Sonochem. 26 (2015) 48–55.
[23] H. Pu, M. Kamruzzaman, D.W. Sun, Selection of feature wavelengths for developing multispectral imaging systems for quality, safety and authenticity of muscle foods-A review, Trends Food Sci. Technol. 45 (1) (2015) 86–104.
[24] A. Nakonieczna, B. Paszkowski, A. Wilczek, A. Szypłowska, W. Skierucha, Electrical impedance measurements for detecting artificial chemical additives in liquid food products, Food Control 66 (2016) 116–129.
[25] S. Trabelsi, M.A. Lewis, S.O. Nelson, Microwave moisture meter for in-shell peanut kernels, Food Control 66 (2016) 283–290.
[26] G.G.B. Nielsen, A. Kjær, B. Klösgen, P.L. Hansen, A.C. Simonsen, B. Jørgensen, Dielectric spectroscopy for evaluating dry matter content of potato tubers, J. Food Eng. 189 (2016) 9–16.
[27] M. Asad, S.A. Neyadi, O.A. Aidaros, M. Khalil, M. Hussein, Single port bio-sensor design using metamaterial split ring resonator, 2016 5th Int. Conf. on Electronic Devices, Systems and Applications (ICEDSA) (2016) 1–4, http://dx.doi.org/10.1109/ICEDSA.2016.7818515.
[28] C. Sabah, F. Dincer, M. Karaaslan, M. Bakir, E. Unal, O. Akgol, Biosensor applications of chiral metamaterials for marrowbone temperature sensing, J. Electromag. Waves Appl. 29 (17) (2015) 2393–2403.
[29] B. Camli, E. Kusakci, B. Lafci, S. Salman, H. Torun, A.D. Yalcinkaya, Cost-effective microstrip antenna driven ring resonator microwave biosensor for biospecific detection of glucose, IEEE J. Sel. Top. Quantum Electron. 23 (2) (2017) 404–409.
[30] C. Sabah, O.T. Kucuksari, G.T. Sayan, Metamaterial absorber-based sensor embedded into X-band waveguide, Electron. Lett. 50 (2014) 15.
[31] A. Sellier, V. Tatiana, A. Lustrac, Resonant circuit model for efficient metamaterial absorber, Opt. Express 21 (106) (2013) A997–A1006.
[32] S. Bhattacharyya, G. Saptarshi, K.V. Srivastava, Equivalent circuit model of an ultra-thin polarization-independent triple band metamaterial absorber, AIP Adv. 4 (9) (2014) 097127.
[33] D. Factorova, Temperature dependence of biological tissues complex permitivity at microwave frequencies, Adv. Electric Electron. Eng. 7 (2008) 354.
[34] N. Bansal, A.S. Dhaliwal, K.S. Mann, Dielectric characterization of rapeseed (Brassica Napus L.) From 10 to 3000MHz, Biosyst. Eng. 143 (2016) 1–8.
[35] M. Bakir, M. Karaaslan, F. Dincer, K. Delihacıoğlu, C. Sabah, Tunable perfect metamaterial absorber and sensor applıcatıons, J. Mater. Sci: Mater. Electron. 27 (2016) 12091–12099.
[36] M.A.B. Adam, Understanding microwave pyrolysis of biomass materials, PhD thesis, University of Nottingham, 2017.
[37] M.K. Bakir, M. Karaaslan, F. Dincer, C. Sabah, U-shaped frequency selective surfaces for single- and dual-band applications together with absorber and sensor configurations, IET Microwave Antennas Propag. 10 (2016) 293–300.
[38] S. Zhang, X. Kou, B. Ling, S. Wang, Dielectric properties of almond kernels associated with radio frequency and microwave pasteurization, Sci. Rep. 7 (2017) 42452.